Journal of Materials Chemistry A

ROYAL SOCIETY OF CHEMISTRY

PAPER

Cite this: *J. Mater. Chem. A*, 2020, **8**, 7713

Catalyzing zinc-ion intercalation in hydrated vanadates for aqueous zinc-ion batteries†

Chaofeng Liu, [a] Meng Tian,[a] Mingshan Wang, [a] Jiqi Zheng,[a] Shuhua Wang,[b] Mengyu Yan,[a] Zhaojie Wang, [a] Zhengmao Yin,[c] Jihui Yang *[a] and Guozhong Cao *[a]

Hydrated vanadium pentoxide (VOH) can deliver a gravimetric capacity as high as 400 mA h g^{-1} owing to the variable valence states of the V cation from 5+ to 3+ in an aqueous zinc ion battery. The incorporation of divalent transition metal cations has been demonstrated to overcome the structural instability, sluggish kinetics, fast capacity degradation, and serious polarization. The current study reveals that the catalytic effects of transition metal cations are probably the key to the significantly improved electrochemical properties and battery performance because of the higher covalent character of 55% in the Cu–O bond in comparison with 32% in the Mg–O bond in the respective samples. Cu(II) pre-inserted VOH (CuVOH) possesses a significantly enhanced intercalation storage capacity, an increased discharge voltage, great transport properties, and reduced polarization, while both VOH and Mg(II) pre-inserted VOH (MgVOH) demonstrate similar electrochemical properties and performances, indicating that the incorporation of Mg cations has little or no impact. For example, CuVOH has a redox voltage gap of 0.02 V, much smaller than 0.25 V for VOH and 0.27 V for MgVOH. CuVOH shows an enhanced exchange current density of 0.23 A g^{-1}, compared to 0.20 A g^{-1} for VOH and 0.19 A g^{-1} for MgVOH. CuVOH delivers a zinc ion storage capacity of 379 mA h g^{-1}, higher than 349 mA h g^{-1} for MgVOH and 337 mA h g^{-1} for VOH at 0.5 A g^{-1}. CuVOH shows an energy efficiency of 72%, superior to 53% for VOH and 55% for MgVOH. All of the results suggest that pre-inserted Cu(II) cations played a critical role in catalyzing the zinc ion intercalation reaction, while the Mg(II) cations did not exert a detectable catalytic effect.

Received 7th February 2020
Accepted 19th March 2020

DOI: 10.1039/d0ta01468k

rsc.li/materials-a

Introduction

Further development of efficient energy conversion technologies to harvest renewable energy from sunlight, biomass, wind and tide energy has attracted significant attention because of the increasing energy demand and environmental concerns owing to the population explosion and surging industrial development in modern society.[1–3] Energy storage systems (EESs) are one of the important enablers. Rechargeable batteries and supercapacitors are the two main categories in EESs, the former stores the electricity as chemical energy through a redox reaction in their electrode materials and the later utilizes the fast physical adsorption of ions on the surface of the electrode materials.[4–6] The differences in the charge storage mechanism endow batteries with high energy densities and supercapacitors with high power densities.[4,7,8] For example, the mature Li-ion batteries promote the popularity of smart electronics and electric vehicles in modern society owing to their energy densities exceeding 250 W h kg^{-1}, even though the challenges in interface issues and safety, as well as reliability, still remain.[9,10] Aqueous zinc ion batteries (ZIBs) have become a viable member of the EESs because the nonflammable electrolytes ensure their operating safety, the redox reaction provides a moderate energy density, and feasible de-solvation and rapid diffusion of zinc ions in the active materials guarantees their high power densities.[11–14] In comparison with the nonaqueous Li- or Na-ion batteries, ZIBs are safer and more cost effective. To improve the competitiveness of ZIBs in terms of the energy density, the search for cathode materials with a high discharge voltage and large storage capacity has becomes an important priority. Currently, the most commonly investigated cathode materials for ZIBs include manganese oxides,[15–24] vanadium oxides,[25–34] Prussian blue and its analogs,[35–38] transition metal sulfides[39–41] and organic compounds.[42] In manganese dioxides, an essential member of the Mn-based cathodes, the stacking of the [MnO_6] polyhedra provides different chemical activities and ion diffusion channels.[43,44] The partially irreversible phase transition and dissolution of Mn^{3+} cause a rapid capacity degradation,[45,46] though they display a relatively high

[a]*Department of Materials Science and Engineering, University of Washington, Seattle, WA, 98195, USA. E-mail: jihuiy@uw.edu; gzcao@uw.edu*

[b]*Institute of Crystal Materials, Shandong University, Jinan, 250100, China*

[c]*College of Materials Science and Engineering, Qingdao University of Science and Technology, Qingdao, 266042, China*

† Electronic supplementary information (ESI) available. See DOI: 10.1039/d0ta01468k

working voltage around 1.3 V.[15] Prussian blue and its analogs have an open framework beneficial to fast ion diffusion, but the less variable chemical state of the redox ions limits their specific capacity to less than 100 mA h g^{-1}.[36] The weak van der Waals interactions between the layers of the metallic sulfides facilitate zinc ion diffusion, but the serious voltage polarization in the charging/discharging processes leads to a lower battery energy efficiency that limits their practicability.[39,41] The organic compound calix[4]quinone (C4Q), as a promising cathode candidate, displays a safe and flat working voltage of 1 V, and a low polarization of 70 mV; however, the dissolution of discharge products remains a challenge.[42] Vanadium oxides and their hydrates attract more attention owing to their high specific capacity up to 400 mA h g^{-1}, high power density enabled by a fast ion diffusion in the crystalline lattice, and low cost owing to the abundance of vanadium in the Earth's crust.[26,29,30,33,47–50] Layered V_2O_5 chunks exfoliate to thin layers which increase the active sites and present an increased specific capacity in the cycling process[26] and the structural water in the graphene/V_2O_5 composite shields the electrostatic interactions between cations and accelerates zinc ion transport, leading to an impressive power density in the battery.[29,51] Alkali(ne) pre-inserted hydrated vanadium pentoxide effectively expands the lattice spacing to provide a highway for ion diffusion in the electrochemical processes.[31,47,52] These approaches overcome either the structural instability or sluggish kinetics, but seldom triumph over both challenges together. Transition metal (TM) compounds are used as catalysts for oxygen and hydrogen generation owing to the electrons in their 3d orbitals[53] and the electrochemical catalytic effect is widely introduced into Li–S batteries to restrain the dissolution of polysulfides.[54,55] However, the impacts of transition metal cations on hydrated vanadium pentoxides are not clear, especially the stabilizing and catalytic effects on Zn-ion storage reactions.

Our earlier work has demonstrated that Mn(II) cations as structural pillars expand the lattice spacing of VOH to accelerate the ion diffusion and stabilize the crystal structure, promoting energy efficiency with an increase of 70% and a capacity retention of around 92% at 4 A g^{-1} over 2000 cycles.[56] This study compares Cu(II) pre-inserted hydrated vanadium pentoxides (CuVOH) with pure VOH and Mg(II) pre-inserted VOH (MgVOH), and reveals that chemically pre-inserted Cu(II) cations catalyze the redox reaction and improve the reactive kinetics with significantly less polarization, resulting in a much improved battery performance including increased energy and power densities, better cycling stability and a higher energy conversion efficiency.

Experimental

All chemicals were used as received without purification. 2 mmol of V_2O_5 (Sigma-Aldrich) was dissolved into 50 mL of deionized (DI) H_2O with 2 mL of H_2O_2 (30%, Fisher chemical), and 1 mmol of $CuSO_4 \cdot 5H_2O$ (Fisher Scientific) was dissolved separately into 30 mL of DI water. The two solutions were admixed and transferred to a 100 mL Teflon lined stainless steel autoclave and heated to 120 °C and kept at this temperature for 6 h. Brick red precipitates were collected by centrifugation and washed using water and ethanol three times. The collected precipitates were dried at 70 °C overnight in an electric oven and turned greenish. The resulting product (CuVOH) was further dried at 120 °C in a vacuum oven. VOH was synthesized using the same procedure and processing conditions without the Cu(II) source, 80 mL of DI water was used in order to attain the same internal reactive pressure in the Teflon bottle. For the Mg(II) stabilized VOH, sulfate salts were used to synthesize the desired samples and the processes were identical to those of the CuVOH synthesis.

Phase identification was carried out using a Bruker X-ray diffractometer (D8 Discover with IμS 2-D detection system) with an accelerating voltage of 50 kV and a working current of 1000 μA. A Renishaw InVia Raman Microscope equipped with a Leica DMIRBE inverted optical microscope was used to obtain the chemical bond information using one of the laser excitation sources at 514 nm. A thermogravimetric analysis/differential scanning calorimeter (TGA/DSC 3+ STAR^e System, Mettler Toledo) was adopted to analyze the water content of the samples within 30–700 °C in a flowing nitrogen gas (50 sccm). The microstructures of the samples were observed using scanning electron microscopy (SEM, FEI Sirion) at a working voltage of 5 kV and scanning transmission electron microscopy (S/TEM, Tecnai G2 F20) with an accelerating voltage of 200 kV. Inductively coupled plasma (ICP, PerkinElmer, Optima2000DV) was used to confirm the content of metal elements in the samples. The surface chemical states of the samples were determined using a Kratos Axis Ultra DLD X-ray photoelectron spectroscopy system (XPS) with an AlKα radiation source that was operated at 10 mA and 15 kV, and with a charge neutralizer. The angle between the specimen normal and the spectrometer was 0°. The chemical surroundings and states in bulk samples were detected using an X-ray absorption near edge structure (XANES) by means of improved laboratory-based instrumentation. The powder samples were admixed with boron nitride (BN) binder and tableted before conducting transmission-mode measurements. Commercial VO_2 and V_2O_5 purchased from Alfa Aesar were confirmed using XRD and used in accordance with the reference standards.

For the electrode preparation, the active material was mixed with conductive carbon and polyvinylidene fluoride (PVDF) binder in a weight ratio of 7 : 2 : 1 in *N*-methyl-2-pyrrolidone (NMP) solvent to obtain a slurry that was pasted onto a current collector (titanium foil). The prepared electrodes were dried in a vacuum oven at 120 °C overnight. The mass loading of the active materials was 3–4 mg cm^{-2}. Zn metal was used as the anode and 80 μL of 3 M zinc trifluoromethanesulfonate (98%, $Zn(CF_3SO_3)_2$) aqueous solution was injected into the batteries as the electrolyte. A glass fiber filter (Whatman, Grade GF/A) was used as the separator. The redox characteristics of cathodes were tested using cyclic voltammetry (CV) on a Solartron electrochemical station (SI 1287) equipped with an electrochemical impedance spectroscopy system (EIS, SI 1260). The galvanostatic charge and discharge tests were conducted using a Neware tester (CT-4008). A galvanostatic intermittent titration technique (GITT) was applied to analyze the reaction resistance

in the electrochemical process and the tests were performed at a current density of 50 mA g^{-1} with a charging and discharging time and interval of 10 min for each step.

Results and discussion

Fig. 1a shows and compares the X-ray diffraction (XRD) patterns of CuVOH, MgVOH and VOH. For VOH, it can be well indexed to $V_2O_5 \cdot 1.6H_2O$ (PDF 40-1296) and the (001) peak at 7.4° corresponds to an interplanar spacing of 11.9 Å, as reported in the literature.[57] CuVOH and MgVOH have similar XRD patterns, matching the two structures reported.[58–60] One is $M_xV_2O_5A_y \cdot nH_2O$, in which M (cations), A (anions) and water reside in the stacked vanadium-oxide double layers.[58] The other is $M_xV_2O_{5+y} \cdot nH_2O$ that also has a layered structure and M cations are believed to replace the protons in the original structure of the layered hydrated vanadic acids using an electrodeposition process with some peaks indexed in the literature.[59,60] The (001) peaks of CuVOH and MgVOH at 7.9 and 6.7° indicate an interplanar spacing of 11.2 and 13.2 Å, respectively. Cu(II) has an ionic radius of 87 pm, very close to 86 pm of Mg(II), thus the radii of the cations are unlikely to be the determining factor for the change in the interplanar spacing. The electronegativities of Cu and Mg are 1.90 and 1.31 on the Pauling scale, respectively, therefore we speculate that different interactions between the cation and VOH induce varied degrees of compactness along the *c*-direction. Although it is believed that the lattice spacing will be expanded when cations are introduced, as reported for the alkali(ne) preinserted VOH,[31,47] the formation of chemical bonds may have various impacts on the interplanar spacing. Raman spectra in Fig. 1b exhibits similar characteristic peaks among all samples. The peaks around 159 cm^{-1} originate from

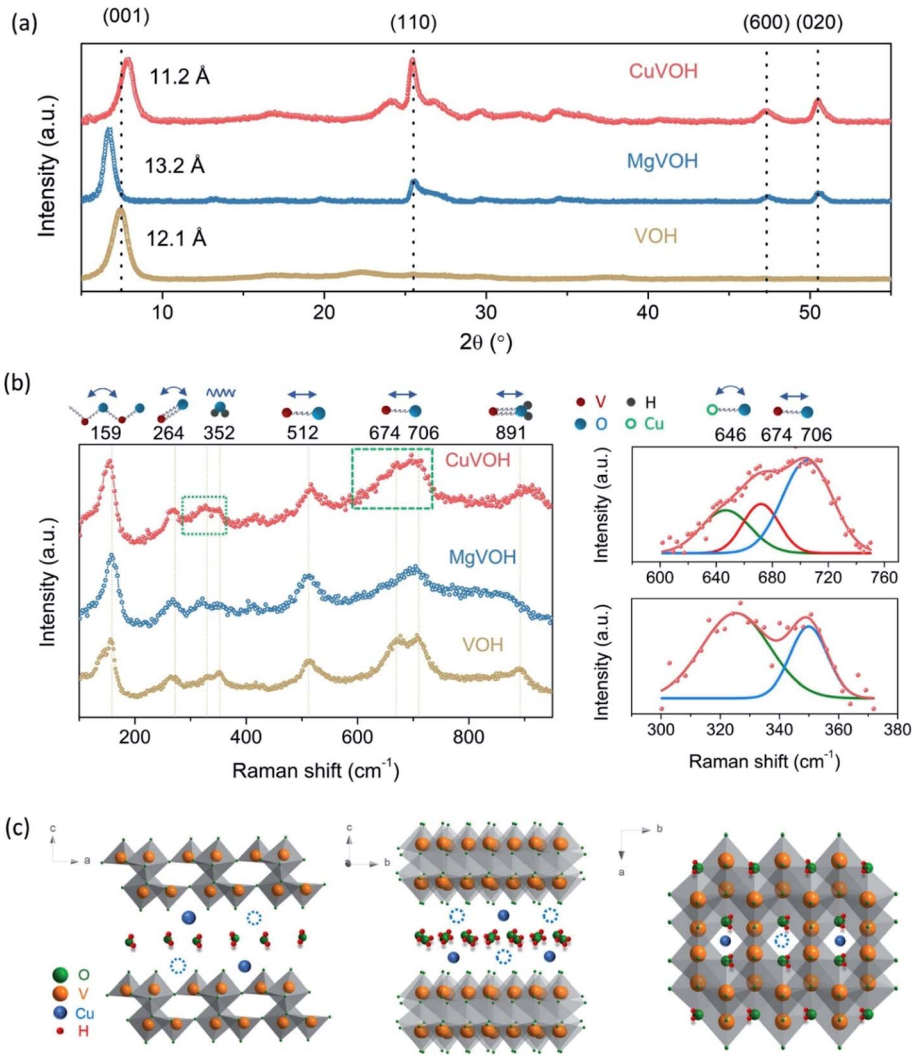

Fig. 1 (a) XRD patterns of three samples with the (001) peak at around 7.4°. VOH samples with chemically inserted divalent cations present similar XRD patterns, although a few minor additional peaks appear in comparison with VOH. (b) Raman spectra of the samples with some peak shifts. The signals from Cu–O bond stretching and vibration suggest that Cu(II) is connected and incorporated into the lattice. (c) A schematic diagram of the possible Cu(II) occupation sites in the framework of VOH based on analysis of the interactions among V, Cu, and O. The probable position for Cu(II) is in the polyhedra built with the bridging O from [VO_5] and water.

the bending vibration of the –V–O–V–O– chains along the *a*-directional and cause a compressive deformation in the planes.[61] The terminal O and center V form a V=O double bond and its bending vibration is reflected by the peak at 264 cm^{-1}.[62] The vibrational motion of the lattice water appears at 352 cm^{-1}. The stretching signal at 512 cm^{-1} comes from a V–O bond in which the O is triply coordinated by V cations and connects three VO_5 pyramids in the lattice.[62,63] Another V–O bond built by a bridging O with two V cations from apical-sharing VO_5 pyramids is manifested by a stretching vibration at 706 cm^{-1} and the disorder of these V–O bonds in the lattice can be detected using the stretching vibration at 674 cm^{-1}.[62,64] The peak at 891 cm^{-1} is attributed to the stretching of V–OH_2, and an upshift in CuVOH means the rotational freedom of water is limited, which might be caused by a strong Cu–O bond consistent with the narrow-spaced (001) planes verified using XRD in Fig. 1a. The green rectangles in the CuVOH spectrum were enlarged and simulated using Lorentz functions. The bending mode of the Cu–O bonds is observed at 646 and 326 cm^{-1}, suggesting the introduced Cu(II) connects to the VO_5 pyramids through a chemical bond[65–67] rather than the weak hydrogen bonds between the water and VO_5 pyramids.[68] The overlap between Cu–O and V_2–O suggests an interaction between Cu(II) and the bridging oxygen in the [VO_5] polyhedral, and that the Cu(II) also interacts with water as shown at 326 cm^{-1} in the Raman spectra. It can be speculated that Cu(II) resides in the polyhedra built using the bridging oxygen and water as shown in Fig. 1c. The electrostatic forces among cations including V^{5+}, V^{4+} and Cu(II) might result in alternative occupations as marked by the solid blue spheres or the dashed blue circles. The overlapping signals of the bending vibration of Mg–O at 855 cm^{-1} [69] with the signal of V–OH_2 at 891 cm^{-1} results in a broad peak in MgVOH, suggesting that chemical bonds also form among Mg(II), water and apical oxygen in the [VO_5] polyhedra. The similarities in the Raman spectra and the differences in XRD patterns suggest CuVOH and MgVOH are likely to have a similar crystal structure as VOH and the introduced divalent cations in the interplane form chemical bonds because of the pre-insertion of cations seldom cause a noticeable difference in the XRD patterns, such as for Li^+ [31] and

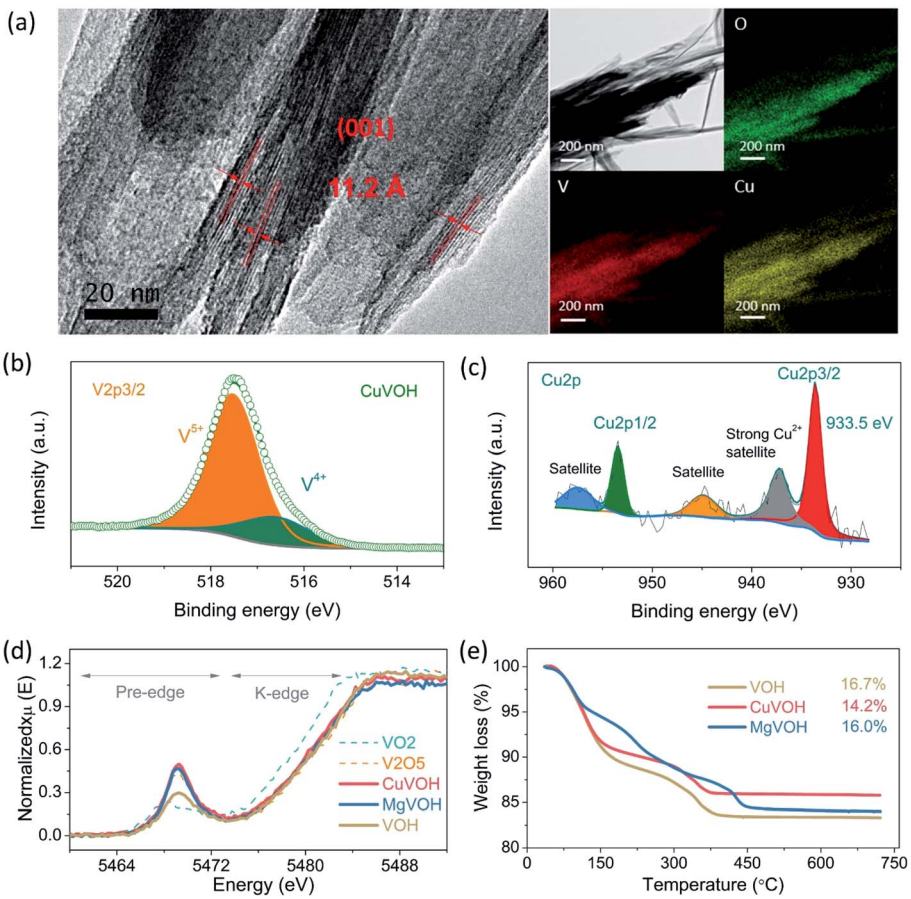

Fig. 2 (a) HRTEM images with the corresponding EDS mapping of CuVOH. The microspheres consist of nanosheets and the lattice spacing is 11.2 Å, which corroborates well with the XRD results. The elements are distributed homogenously in the nanosheets. XPS spectra of (b) V and (c) Cu collected from CuVOH. The appearance of V^{4+} suggests the incomplete oxidation of V^{5+} and the formation of oxygen vacancies. Cu(II) with strong satellite peaks was detected owing to the different local chemical surroundings. (d) Normalized V K-edge XANES spectra of the resulting samples and standard VO_2 and V_2O_5 references. The stronger peak intensities in the pre-edge zone reflect lattice distortion in MgVOH and CuVOH compared with the symmetric coordination in VO_2. (e) TGA curves of the resulting samples collected over a temperature range of 30–700 °C. The three resulting samples have a similar water content of around 16 wt%.

Mg^{2+} [47] pre-insertion. ICP measurements confirm the atomic ratios of Cu : V and Mg : V are 0.091 : 1 and 0.080 : 1, respectively, suggesting the chemical formula of both samples can be written as $Cu_{0.15}V_2O_{5+\delta}\cdot nH_2O$ and $Mg_{0.14}V_2O_{5+\delta}\cdot nH_2O$, respectively. The concentration of the Cu(II) cation in the resulting samples was not adjusted, though the molar ratio of $CuSO_4$ and V_2O_5 was varied from 1 : 20 to 1 : 2. Increasing the concentration of Cu(II) could increase the product yield but not influence the phase (Fig. S1†).

Fig. S2† displays the SEM images, showing all samples have similar microspheres built with nanosheets. The TEM image further reveals that CuVOH has urchin-like microspheres (see inset in Fig. S2a†). The interplanar spacing of 11.2 Å in the high resolution (HR)TEM image (Fig. 2a) is in good agreement with that in between the (001) planes estimated from the XRD pattern (Fig. 1b). Elements are distributed homogeneously as revealed by the energy-dispersive X-ray spectroscopy (EDS) mappings, suggesting the incorporation of Cu(II) in VOH. The high resolution XPS spectrum of V shown in Fig. 2b, reveals the co-existence of both V^{5+} and V^{4+}, with a peak at 517.5 eV from V^{5+} and a smaller peak at 516.6 eV from V^{4+} as reported.[70,71] The amount of V^{4+} is estimated to be 17.9% in CuVOH, higher than the 13.2% in VOH (Fig. S3†). The formation of V^{4+} in VOH is possibly due to the reduction reaction that occurs between V_2O_5 and H_2O_2 to form $VO(O_2)^+$ in the synthesis process.[72] The chemical valence of Cu(II) was also confirmed and the peak at 933.5 eV and the strong satellite peak at 937.2 eV [73, 74] (Fig. 2c) demonstrate no oxidizing reaction occurs on Cu(II). The additional satellite peaks imply an intensive coulombic interaction among the 3d electrons and the hybridization between the Cu 3d and other valence orbitals as observed in other TM compounds,[75–77] especially when the local chemical surrounding involves oxygen that is connected to V or H. The chemical states of the V and Mg cations in MgVOH were also analyzed using XPS and spectra are shown in Fig. S4.† V^{4+} is detected in MgVOH and the amount is approximately 16.5% as listed in Table 1. The XPS spectrum of elemental Mg indicates that its chemical valence remains at 2+, confirming that they are chemically stable in the hydrothermal process. Both samples have a similar amount of V^{4+}. The chemical surroundings and states of the V cations in the bulk samples were tested by means of XANES and the spectra are shown in Fig. 2d. The peak that appeared in the pre-edge region corresponds to the coordination symmetry of the metal ion center and their intensities also reflect the degree of unoccupied d orbitals.[78,79] VO_2 as an empirical standard is built by a highly symmetric [VO_6] octahedron and fewer unoccupied d orbitals are present in V^{4+}, resulting in a lower intensity. Although V_2O_5 consists of asymmetric [VO_5] pyramids and V^{5+} contains more unoccupied d orbitals, it exhibits a higher pre-edge intensity. The intensity of VOH sits between those of VO_2 and V_2O_5, agreeing with a structure that consists of alternate symmetric [VO_6] octahedron and asymmetric [VO_5] pyramids. The intensities of MgVOH and CuVOH are higher than those of VOH and V_2O_5, demonstrating more serious lattice distortion in both samples because of the introduction of the alien cation and the formation of strong chemical bonds as verified using Raman analysis. CuVOH presents a slightly higher intensity that is in accordance with the difference in the amount of V^{4+} tested using XPS as the larger size V^{4+} in the lattice causes a more serious lattice distortion.[80] The K-edge position reflects the chemical states of the V cations, three samples have similar K-edge positions to the empirical standard V_2O_5, suggesting V^{5+} dominates their chemical states. However, a slight shift towards a lower photo energy confirms the formation of V^{4+} in the CuVOH and MgVOH bulks in comparison with VOH as verified using XPS. TGA was performed with a temperature range of 30–700 °C to evaluate the water content in the resulting samples (Fig. 2e). CuVOH has the lowest water content of 14.2 wt%, MgVOH is 16.0 wt% and VOH has the highest one of 16.7 wt%. Considering the deviation in the measurements, it could be assumed that the three resulting samples have a similar water content. These results demonstrate that CuVOH and MgVOH possess similar crystal structures and chemical states, and the possible influences from water on their electrochemical performance can be excluded.

Table 1 Physical parameters of the stabilized VOH

Sample ID	MgVOH	CuVOH
Interplanar spacing of (001) (Å)	13.2	11.2
Ionic radius of the divalent cation (pm)	86 (Mg)	87 (Cu)
Electronegativity of element (Pauling scale)	1.31 (Mg)	1.90 (Cu)
The amount of V^{4+} (%)	16.5	17.9

Cyclic voltammetry (CV) curves are shown in Fig. 3a and two pairs of redox peaks appear within the operating voltage window of 0.2–1.6 V at a sweep rate of 0.1 mV s^{-1}. One pair of peaks around 1.0 V corresponds to the redox reaction of V^{5+}/V^{4+} and the other appears at 0.5 V and comes from the redox pair of V^{4+}/V^{3+}, similar to those observed in V_2O_5 or $V_2O_5\cdot nH_2O$.[26,29] In the first cathodic process of CuVOH (Fig. S5†), the first reduction peak appears at 0.96 V, but shifts to 0.98 V in subsequent cycles. This phenomenon is often observed in vanadates when zinc- or lithium-ions are intercalated, and is commonly ascribed to a slight structural distortion because of the ion insertion or the activation of the fresh electrode.[34,81] The overlap of the second and third cycles implies a high redox reversibility in the CuVOH cathode. The third cycles in the CV curves are used to compare the differences among the samples, and voltage gaps of the redox pairs in all samples are shown in Fig. 3b. The possible redox reaction related to Cu(II) could cause confusion in the working voltage window because Cu(II) will participate in the electrochemical reaction.[82] In fact, Cu(II) in CuO converts to Cu and Cu_2O in the first cycle and then protons insert/extract Cu_2O in the following cycles rather than zinc ions[82] owing to sufficient protons in the electrolyte of the 3 M $ZnSO_4$ aqueous solution (pH < 5.4).[83] In addition, the anodic reaction of Cu^+/Cu^0 occurs around 1.0 V and the cathodic reaction occurs at 0.7 V, leading to a serious voltage hysteresis. Although the CuVOH cathode displays a decreased voltage difference for V^{5+}/V^{4+} of 0.02 V, which is lower than the 0.27 V of MgVOH and 0.25 V of VOH. The reduced voltage difference in CuVOH further verifies that the introduced Cu^{2+} possibly would not participate in the

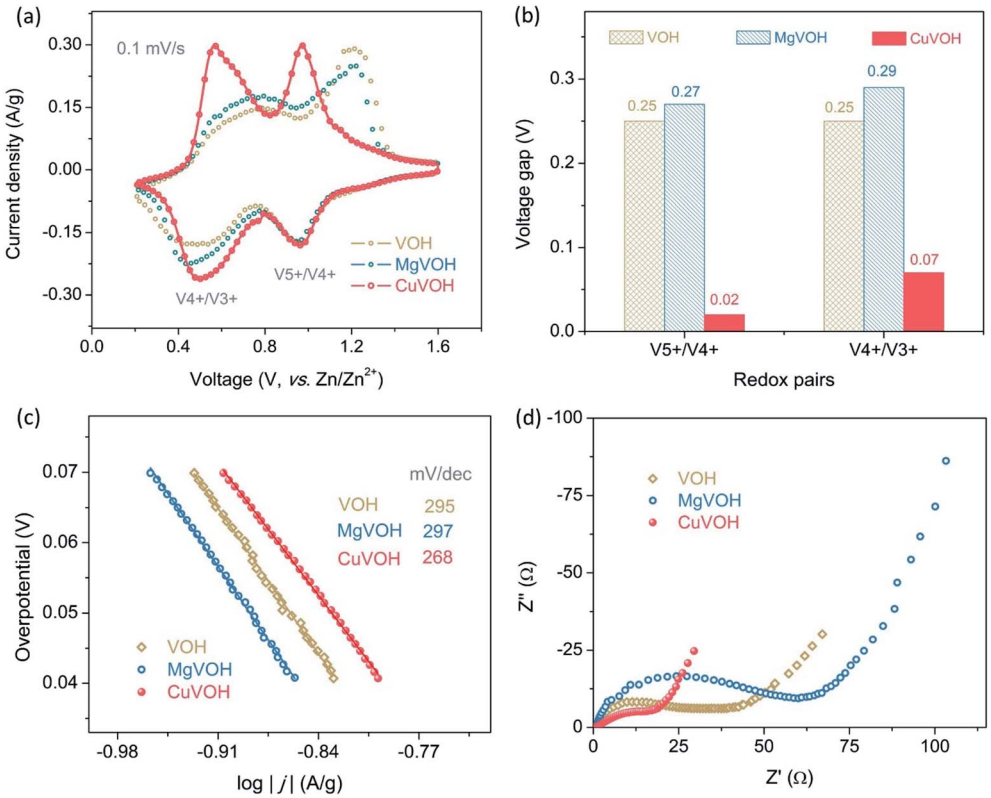

Fig. 3 (a) CV curves from a CuVOH cathode collected at 0.1 mV s^{-1} in an aqueous zinc ion battery. Two pairs of redox peaks originate from the redox reactions of V^{5+}/V^{4+} and V^{4+}/V^{3+}. (b) Voltage gap of the V^{5+}/V^{4+} and V^{4+}/V^{3+} redox couples in different samples; the data were collected from the CV curves tested at 0.1 mV s^{-1}. Cu(II) cations decrease the voltage gaps in comparison with MgVOH and VOH. (c) Tafel curves. The smaller slopes of the curves reflect the better catalytic effects of CuVOH. (d) EIS spectra of three samples.

redox process. An interesting phenomenon is that the V^{5+}/V^{4+} redox pairs exhibit a slightly smaller voltage gap of 0.02 V compared to the V^{4+}/V^{3+} redox pair (0.07 V) in the CuVOH cathode. One possible reason is that less Zn^{2+} is inserted into the host lattice corresponding to the V^{5+}/V^{4+} redox pairs and there are sufficient channels for ion diffusion at this stage. The other is that V^{4+} and V^{3+} have a larger ionic radii of 72 and 78 pm in the six-coordination than that (68 pm) of V^{5+} in the same surroundings,[84] the larger ionic radii of cations distributed in the layers randomly block the Zn ion migration, leading to a high energy barrier for Zn-ion diffusion and slower reaction kinetics. To further explore the functions of the Cu(II) cation, potentiostatic polarization curves were tested at a sweep rate of 0.1 mV s^{-1} (Fig. S6†) and the corresponding Tafel curves are plotted as shown in Fig. 3c. The slopes of the Tafel curves decrease from 295 mV dec^{-1} of VOH, 297 mV dec^{-1} of MgVOH to 268 mV dec^{-1} of CuVOH, and the corresponding exchange current density increase from 0.20 A g^{-1} of VOH and 0.19 A g^{-1} of MgVOH to 0.23 A g^{-1} of CuVOH. The enhanced current density can be attributed to the catalytic effect of Cu(II) cations in promoting the zinc-ion storage reaction because the partially unfilled 3d orbitals of transition metal cations can capture and transfer electrons to accelerate the redox reaction. Elemental Cu has an electronegativity of 1.90 Pauling units, while the Mg element is 1.31 Pauling units. The covalent character of the chemical bonds consisting of cations and oxygen in a compound can be evaluated using the following equation:[75]

$$\%\ \text{covalent character} = 100 \times \exp[-0.25(X_M - X_O)^2] \quad (1)$$

In which X_M and X_O are Pauling electronegativities of metallic and oxygen (3.44 Pauling units) elements, respectively. The covalent character in the Cu–O bond is 55% in CuVOH, while it

Table 2 Comparison of the electrochemical kinetics of three samples

Sample ID	VOH	MgVOH	CuVOH
Specific capacity at 0.5 A g^{-1} (mA h g^{-1})	337	349	379
Exchange current density (A g^{-1})	0.20	0.19	0.23
Charge transfer resistance (Ω)	40	59	16
Ion diffusion coefficient (cm^2 s^{-1})	3.3×10^{-13}	2.0×10^{-13}	1.6×10^{-12}

is around 32% in the Mg–O bond. A higher covalence character in the chemical bond enables a stronger catalytic effect owing to the high electron sharing and the feasible electron transfer in the reaction process.[85,86] To further confirm the catalytic effect of Cu(II), the EIS spectra in Fig. 3d compares the charge transfer resistances, CuVOH has the smallest resistance of 16 Ω in comparison with 40 Ω of VOH and 59 Ω of MgVOH, in agreement with the enhanced reaction kinetics disclosed by CV curves. The linear relationship between the frequency and real resistance in Fig. S7† reveals the ion diffusion coefficients of three samples, CuVOH presents the highest ion diffusion coefficient of 15.5×10^{-13} cm^2 s^{-1} compared to 3.3×10^{-13} cm^2 s^{-1} of VOH and 2.0×10^{-13} cm^2 s^{-1} of MgVOH. The enhanced reaction kinetics, manifested by the exchange current density, charge transfer resistance and ion diffusion coefficient, as listed in Table 2, demonstrate that Cu(II) with 3d orbitals plays a role

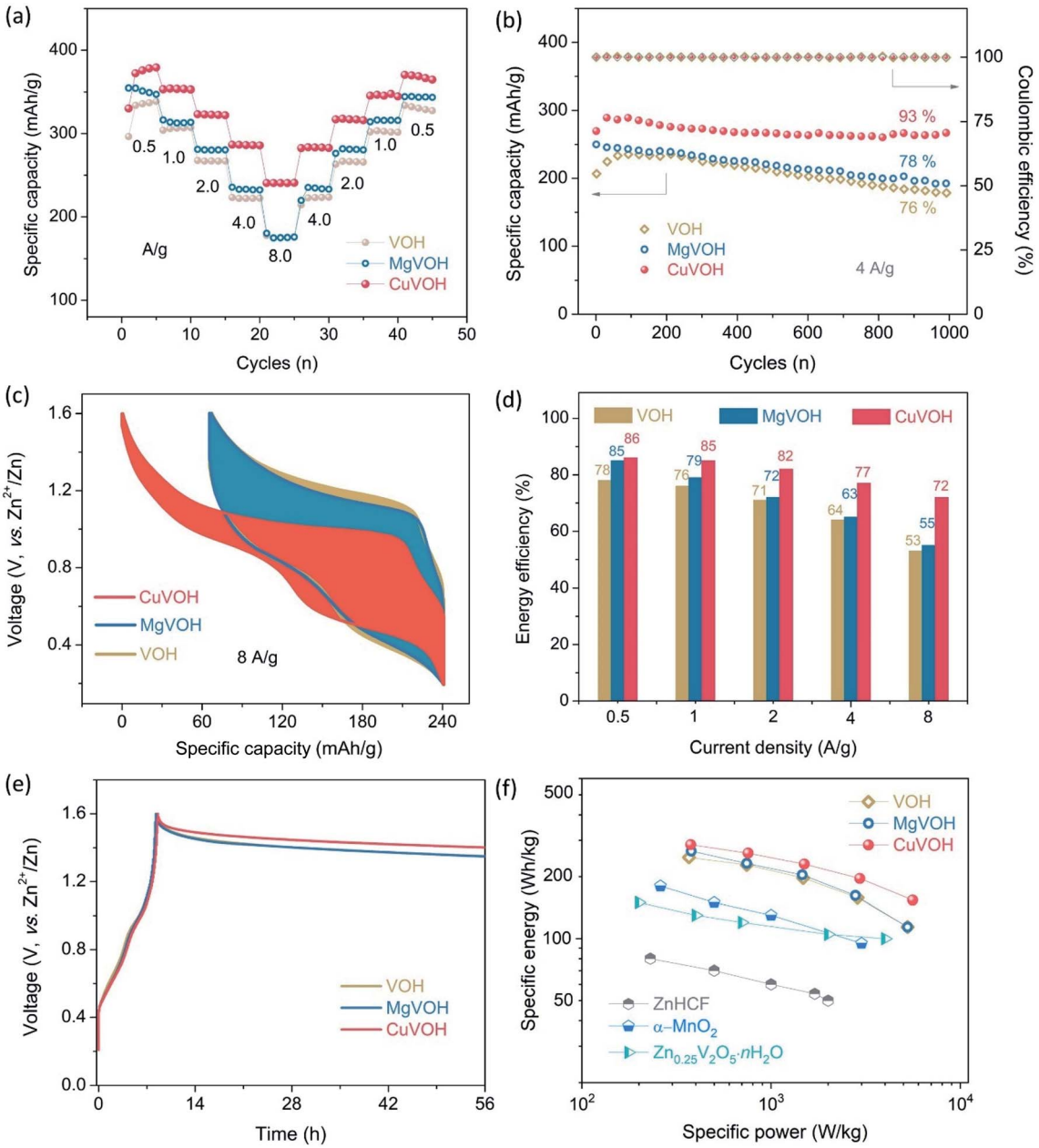

Fig. 4 (a) Rate capabilities and (b) cycling stabilities with the corresponding coulombic efficiencies at 4 A g^{-1} for all cathodes. The improved rate capabilities and enhanced capacities are attributed to the stabilized crystal structure and catalytic effect enabled by the Cu(II) cations. (c) Voltage hysteresis of the cathodes collected at 8 A g^{-1}. The area encompassed by the charge/discharge curves is the energy loss in one cycle. (d) Comparison of energy efficiencies at different rates. MgVOH and VOH present similar EEs under the same conditions, but CuVOH has the highest efficiency, suggesting a catalytic effect from the transition metal cation Cu(II) that promotes efficient redox reactions. (e) Voltage degradation after being fully charged. CuVOH presents higher voltage retention after 48 h on the shelf. (f) Ragone plots of the cathodes in this study compared with reported results (α-MnO_2,[88] ZnHCF[89] and $Zn_{0.25}V_2O_5 \cdot nH_2O$[49]).

as a catalyst to accelerate the Zn-ion intercalation in aqueous batteries.

Fig. 4a compares the rate capabilities of three cathodes, CuVOH delivers the highest specific capacity at 379 mA h g^{-1}, compared to MgVOH at 349 mA h g^{-1} and VOH of 337 mA h g^{-1} at 0.5 A g^{-1}. CuVOH achieves a capacity retention of 93% over 1000 cycles, compared to 76% of VOH and 78% of MgVOH (Fig. 4b), much better than the data reported in the literature listed in Table S1.† Fig. 4c shows the voltage hysteresis of three cathodes at 8 A g^{-1} and the areas encompassed by the charging and discharging curves are the energy loss in each charge–discharge cycle. The small hysteresis in CuVOH corroborate the narrow voltage gap observed in the CV curve in Fig. 3a and b, resulting in a much higher energy conversion efficiency than those of both MgVOH and VOH. The energy efficiency (EE) is defined by the ratio of the discharged and charged energy density of a given battery and reflects the energy conversion loss caused by polarization and side reactions in practice.[87] Fig. 4d compares the energy efficiencies (EEs) of batteries at different current densities. At the small current density, the batteries display similar EEs, such as 85% of MgVOH and 86% of CuVOH, because a considerably sufficient reaction occurs with thorough diffusion. When the current density is increased to 8 A g^{-1}, the EE of CuVOH remains at 72%, but MgVOH and VOH have the values of 55% and 53%, respectively. When the batteries were fully charged at 50 mA g^{-1} and put on the shelf for over 48 h, the voltage of CuVOH remained at 1.41 V which is higher than the 1.35 V of MgVOH and VOH (Fig. 4e). The maximum energy and power density of CuVOH are 286 W h kg^{-1} and 5600 W kg^{-1}, respectively, as shown in Fig. 4f. It displays a competitive practicability compared to MgVOH (E_{max}: 266 W h kg^{-1}, P_{max}: 5262 W kg^{-1}), and VOH (E_{max}: 248 W h kg^{-1}, P_{max}: 5261 W kg^{-1}) as well as the reported results (α-MnO_2,[88] ZnHCF[89] and $Zn_{0.25}$-$V_2O_5 \cdot nH_2O$[49]). In their crystal structures, CuVOH has the smallest lattice spacing of 11.2 Å amongst all of the samples, but delivers the best rate capability, suggesting that the lattice spacing is not the only limiting factor to determine the electrochemical performance of VOH.

To further confirm the catalytic effect, the reaction resistance and mechanism of both samples were studied through GITT and *ex situ* XRD tests. The relaxation rest after the charging and discharging process causes the zigzag profiles in the GITT plot (Fig. 5a), and the voltage recovery is usually used to estimate the ion diffusion and *IR* drop reflects the reaction resistances.[56] Based on the GITT curves, the diffusion coefficient of the zinc ion in the material can be calculated using the following equation:[47]

$$D_{Zn^{2+}} = \frac{4}{\pi}\left(\frac{n_M V_M}{S}\right)^2 \left[\frac{\Delta E_s}{\tau\left(\frac{dE_\tau}{d\sqrt{\tau}}\right)}\right]^2 \quad (\tau \ll L^2/D_{Zn^{2+}}) \qquad (2)$$

In which τ is the interval of 10 min for each step; n_M and V_M are the moles (mol) of the material and molar volume (cm^3 mol^{-1}), respectively; S is the electrode–electrolyte contact area (cm^2); ΔE_s and ΔE_τ are the changes in the steady state voltage and

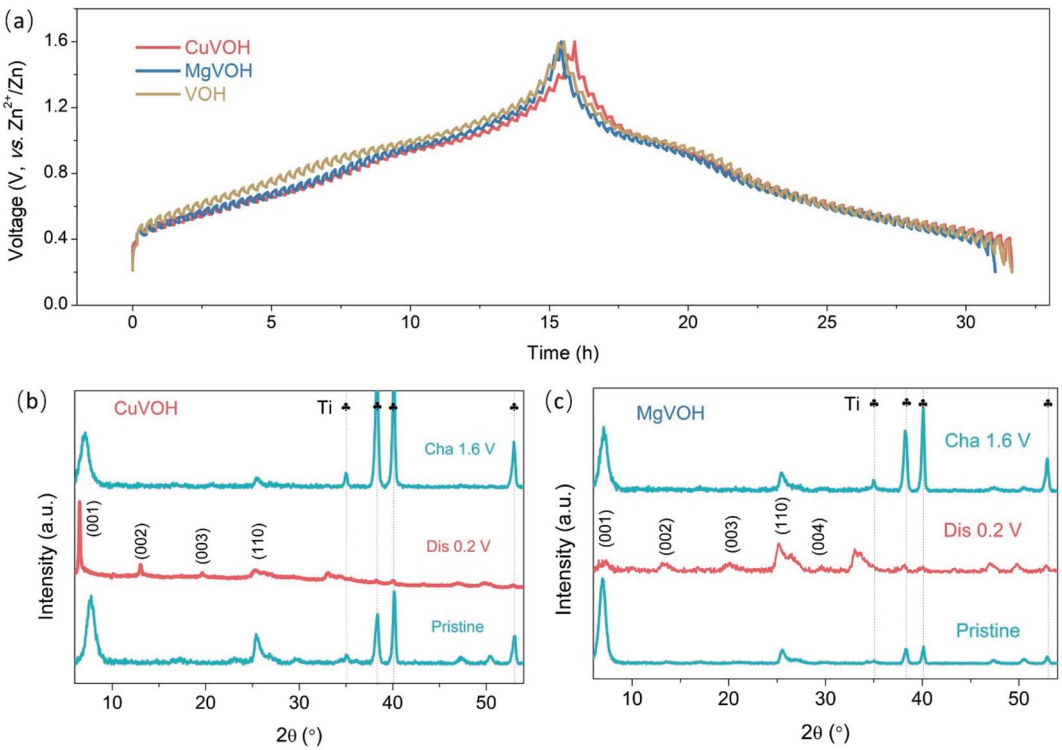

Fig. 5 (a) GITT plots of the cathodes collected at a current density of 50 mA g^{-1} with a charge/discharge time and interval of 10 min for each step. *Ex situ* XRD patterns of (b) CuVOH and (c) MgVOH; the phase evolution suggests a similar phase transition occurred in both cathodes in the charge/discharge process.

overall cell voltage after applying a current pulse in a single step without an *IR* drop, respectively. L is the thickness of the electrode. When the variation of the voltage (ΔE_τ) in the titration process was found to show a linear relationship against $\tau^{1/2}$, the equation can be simplified as below:[47]

$$D_{Zn^{2+}} = \frac{4}{\pi}\left(\frac{n_M V_M}{S}\right)^2\left[\frac{\Delta E_s}{\Delta E_\tau}\right]^2 \quad (3)$$

The molar volume is one of most important parameters for the calculation of the diffusion coefficient. However, studies on the crystal structure of the resulting samples using synchrotron radiation techniques face challenges from the vanadium and water. To avoid a misleading comparison among the three samples, the diffusion coefficients from GITT at the current stage are not calculated. By contrast, EIS collected at the same conditions are reasonable[90] for comparing their diffusion as listed in Table 2. In addition, VOH presents the largest *IR* drop and the highest charging voltage, implying the sluggish reaction kinetics. Cu(II) and Mg(II) connects the [VO_n] layers to build a three-dimensional network for charge transfer compared to the two-dimensional VOH. However, the ionically dominated Mg–O bonds localize the electrons and a stronger electrostatic attraction suppresses the electron transfer, resulting in a higher *IR* in comparison with that of CuVOH as shown in Fig. S8,† in agreement with the smallest charge transfer resistance in Fig. 3e and Table 2. The phases at the fully discharged and charged states were checked using *ex situ* XRD measurements (Fig. 5b and c), and the pristine phase can be totally recovered in the fully charged states. In the fully discharged state, several peaks appeared because of the highly ordered layers of stacking formed by the strong chemical connection built by intercalated Zn ions. The additional peaks can be indexed well with the preinserted VOH as reported.[47] A slight distinction is that the (001) peak in CuVOH shifts to lower angles and a weaker peak intensity is revealed in MgVOH. The possible reason for this can be attributed to the characteristics of the chemical bonds. Covalently dominated Cu–O bonds enable the lattice flexibility to accommodate the volume expansion without crystallinity damage, although the ionically dominated Mg–O bonds easily lose the buffering function when zinc ion inserted. This is consistent with the cycling stability at a high rate of 4 A g^{-1} as shown in Fig. 4b. The reversible phase transition with a similar intercalation mechanism in both cathodes and the different electrochemical performance further indicate a catalytic effect from the special electron structure of Cu(II). The partially unfilled 3d orbitals can capture and transfer electrons in the redox reactions as expected from a catalytic function and promote the Zn-ion storage reaction kinetics in aqueous batteries.

Conclusions

Chemically pre-inserted divalent Cu and Mg in hydrated vanadium pentoxides form chemical bonds to connect the adjacent [VO_5] layers and render a robust framework for reversible zinc ion intercalation. The enhanced exchange current density, reduced charge transfer resistance and increased covalent character in CuVOH, as compared to MgVOH and VOH, result in an improved rate capability, a reduced voltage gap and enhanced energy efficiency. CuVOH offers a specific capacity of 379 mA h g^{-1}, as compared to 349 mA h g^{-1} for MgVOH and 337 mA h g^{-1} for VOH at 0.5 A g^{-1}. In distinct contrast, preinserted Mg exerts limited influence on the electrochemical properties and the performance of the batteries. The significantly enhanced electrochemical properties and battery performance of CuVOH are probably attributed to the catalytic effects of the transition metal cation Cu(II). This strategy is effective and efficient for designing and exploring high-performance cathode materials for multi-valent ion batteries.

Conflicts of interest

There are no conflicts to declare.

Acknowledgements

This work was supported by the National Science Foundation (CBET-1803256). Part of this work was conducted at the Molecular Analysis Facility, a National Nanotechnology Coordinated Infrastructure site at the University of Washington, which is supported in part by the National Science Foundation (grant NNCI-1542101), the University of Washington, the Molecular Engineering & Sciences Institute, and the Clean Energy Institute. CL acknowledges Neware Battery Testing Instruments for providing technical support. MY and JY acknowledge support from The Clean Energy Institute (CEI) at the University of Washington and the Inamori Foundation.

References

1 S. Chu, Y. Cui and N. Liu, *Nat. Mater.*, 2016, **16**, 16–22.
2 G. Crabtree, *Nature*, 2015, **526**, S92.
3 Z. P. Cano, D. Banham, S. Ye, A. Hintennach, J. Lu, M. Fowler and Z. Chen, *Nat. Energy*, 2018, **3**, 279–289.
4 P. Simon, Y. Gogotsi and B. Dunn, *Science*, 2014, **343**, 1210–1211.
5 M. Winter and R. J. Brodd, *Chem. Rev.*, 2004, **104**, 4245–4270.
6 C. Liu, Z. G. Neale and G. Cao, *Mater. Today*, 2016, **19**, 109–123.
7 C. Liu, F. Li, L. P. Ma and H. M. Cheng, *Adv. Mater.*, 2010, **22**, E28–E62.
8 C. M. Hayner, X. Zhao and H. H. Kung, *Annu. Rev. Chem. Biomol. Eng.*, 2012, **3**, 445–471.
9 K. Liu, Y. Liu, D. Lin, A. Pei and Y. Cui, *Sci. Adv.*, 2018, **4**, eaas9820.
10 C. Liu, J. Yuan, R. Masse, X. Jia, W. Bi, Z. Neale, T. Shen, M. Xu, M. Tian, J. Zheng, J. Tian and G. Cao, *Adv. Mater.*, 2020, DOI: 10.1002/adma.201905245.
11 A. Konarov, N. Voronina, J. H. Jo, Z. Bakenov, Y. K. Sun and S. T. Myung, *ACS Energy Lett.*, 2018, **3**, 2620–2640.
12 Y. Li, J. Fu, C. Zhong, T. Wu, Z. Chen, W. Hu, K. Amine and J. Lu, *Adv. Energy Mater.*, 2019, **9**, 1802605.

13 J. F. Parker, J. S. Ko, D. R. Rolison and J. W. Long, *Joule*, 2018, **2**, 2519–2527.
14 Y. Liu, C. Li, J. Xu, M. Ou, C. Fang, S. Sun, Y. Qiu, J. Peng, G. Lu, Q. Li, J. Han and Y. Huang, *Nano Energy*, 2019, **67**, 104211.
15 H. Pan, Y. Shao, P. Yan, Y. Cheng, K. S. Han, Z. Nie, C. Wang, J. Yang, X. Li, P. Bhattacharya, K. T. Mueller and J. Liu, *Nat. Energy*, 2016, **1**, 16039.
16 L. Wang, X. Cao, L. Xu, J. Chen and J. Zheng, *ACS Sustainable Chem. Eng.*, 2018, **6**, 16055–16063.
17 Y. Fu, Q. Wei, G. Zhang, X. Wang, J. Zhang, Y. Hu, D. Wang, L. Zuin, T. Zhou, Y. Wu and S. Sun, *Adv. Energy Mater.*, 2018, **8**, 1801445.
18 B. Lee, H. R. Lee, H. Kim, K. Y. Chung, B. W. Cho and S. H. Oh, *Chem. Commun.*, 2015, **51**, 9265–9268.
19 M. Chamoun, W. R. Brant, C. W. Tai, G. Karlsson and D. Noréus, *Energy Storage Materials*, 2018, **15**, 351–360.
20 S. Islam, M. H. Alfaruqi, V. Mathew, J. Song, S. Kim, S. Kim, J. Jo, J. P. Baboo, D. T. Pham, D. Y. Putro, Y. K. Sun and J. Kim, *J. Mater. Chem. A*, 2017, **5**, 23299–23309.
21 C. Zhu, G. Fang, J. Zhou, J. Guo, Z. Wang, C. Wang, J. Li, Y. Tang and S. Liang, *J. Mater. Chem. A*, 2018, **6**, 9677–9683.
22 W. Sun, F. Wang, S. Hou, C. Yang, X. Fan, Z. Ma, T. Gao, F. Han, R. Hu, M. Zhu and C. Wang, *J. Am. Chem. Soc.*, 2017, **139**, 9775–9778.
23 G. G. Yadav, J. W. Gallaway, D. E. Turney, M. Nyce, J. Huang, X. Wei and S. Banerjee, *Nat. Commun.*, 2017, **8**, 14424.
24 G. Liu, H. Huang, R. Bi, X. Xiao, T. Ma and L. Zhang, *J. Mater. Chem. A*, 2019, **7**, 20806–20812.
25 P. Hu, M. Yan, T. Zhu, X. Wang, X. Wei, J. Li, L. Zhou, Z. Li, L. Chen and L. Mai, *ACS Appl. Mater. Interfaces*, 2017, **9**, 42717–42722.
26 N. Zhang, Y. Dong, M. Jia, X. Bian, Y. Wang, M. Qiu, J. Xu, Y. Liu, L. Jiao and F. Cheng, *ACS Energy Lett.*, 2018, **3**, 1366–1372.
27 Q. Pang, C. Sun, Y. Yu, K. Zhao, Z. Zhang, M. Voyles Paul, G. Chen, Y. Wei and X. Wang, *Adv. Energy Mater.*, 2018, **8**, 1800144.
28 P. Senguttuvan, S. D. Han, S. Kim, A. L. Lipson, S. Tepavcevic, T. T. Fister, I. D. Bloom, A. K. Burrell and C. S. Johnson, *Adv. Energy Mater.*, 2016, **6**, 1600826.
29 M. Yan, P. He, Y. Chen, S. Wang, Q. Wei, K. Zhao, X. Xu, Q. An, Y. Shuang, Y. Shao, K. T. Mueller, L. Mai, J. Liu and J. Yang, *Adv. Mater.*, 2018, **30**, 1703725.
30 L. Chen, Y. Ruan, G. Zhang, Q. Wei, Y. Jiang, T. Xiong, P. He, W. Yang, M. Yan, Q. An and L. Mai, *Chem. Mater.*, 2019, **31**, 699–706.
31 Y. Yang, Y. Tang, G. Fang, L. Shan, J. Guo, W. Zhang, C. Wang, L. Wang, J. Zhou and S. Liang, *Energy Environ. Sci.*, 2018, **11**, 3157–3162.
32 X. Dai, F. Wan, L. Zhang, H. Cao and Z. Niu, *Energy Storage Materials*, 2018, **17**, 143–150.
33 P. Hu, T. Zhu, X. Wang, X. Wei, M. Yan, J. Li, W. Luo, W. Yang, W. Zhang, L. Zhou, Z. Zhou and L. Mai, *Nano Lett.*, 2018, **18**, 1758–1763.
34 V. Soundharrajan, B. Sambandam, S. Kim, M. H. Alfaruqi, D. Y. Putro, J. Jo, S. Kim, V. Mathew, Y. K. Sun and J. Kim, *Nano Lett.*, 2018, **18**, 2402–2410.
35 Z. Liu, G. Pulletikurthi and F. Endres, *ACS Appl. Mater. Interfaces*, 2016, **8**, 12158–12164.
36 R. Trócoli and F. La Mantia, *ChemSusChem*, 2015, **8**, 481–485.
37 G. Kasiri, R. Trócoli, A. Bani Hashemi and F. La Mantia, *Electrochim. Acta*, 2016, **222**, 74–83.
38 L. Zhang, L. Chen, X. Zhou and Z. Liu, *Sci. Rep.*, 2015, **5**, 18263.
39 H. Li, Q. Yang, F. Mo, G. Liang, Z. Liu, Z. Tang, L. Ma, J. Liu, Z. Shi and C. Zhi, *Energy Storage Materials*, 2019, **19**, 94–101.
40 T. Jiao, Q. Yang, S. Wu, Z. Wang, D. Chen, D. Shen, B. Liu, J. Cheng, H. Li, L. Ma, C. Zhi and W. Zhang, *J. Mater. Chem. A*, 2019, **7**, 16330–16338.
41 W. Xu, C. Sun, K. Zhao, X. Cheng, S. Rawal, Y. Xu and Y. Wang, *Energy Storage Materials*, 2019, **16**, 527–534.
42 Q. Zhao, W. Huang, Z. Luo, L. Liu, Y. Lu, Y. Li, L. Li, J. Hu, H. Ma and J. Chen, *Sci. Adv.*, 2018, **4**, eaao1761.
43 B. Tang, L. Shan, S. Liang and J. Zhou, *Energy Environ. Sci.*, 2019, **12**, 3288–3304.
44 M. Song, H. Tan, D. Chao and H. J. Fan, *Adv. Funct. Mater.*, 2018, **28**, 1802564.
45 G. Fang, C. Zhu, M. Chen, J. Zhou, B. Tang, X. Cao, X. Zheng, A. Pan and S. Liang, *Adv. Funct. Mater.*, 2019, **29**, 1808375.
46 S. Zhao, B. Han, D. Zhang, Q. Huang, L. Xiao, L. Chen, D. G. Ivey, Y. Deng and W. Wei, *J. Mater. Chem. A*, 2018, **6**, 5733–5739.
47 F. Ming, H. Liang, Y. Lei, S. Kandambeth, M. Eddaoudi and H. N. Alshareef, *ACS Energy Lett.*, 2018, **3**, 2602–2609.
48 X. Guo, G. Fang, W. Zhang, J. Zhou, L. Shan, L. Wang, C. Wang, T. Lin, Y. Tang and S. Liang, *Adv. Energy Mater.*, 2018, **8**, 1801819.
49 D. Kundu, B. D. Adams, V. Duffort, S. H. Vajargah and L. F. Nazar, *Nat. Energy*, 2016, **1**, 16119.
50 D. Chao, C. Zhu, M. Song, P. Liang, X. Zhang, N. H. Tiep, H. Zhao, J. Wang, R. Wang, H. Zhang and H. J. Fan, *Adv. Mater.*, 2018, **30**, 1803181.
51 T. Wu, K. Zhu, C. Qin and K. Huang, *J. Mater. Chem. A*, 2019, **7**, 5612–5620.
52 J. Zheng, C. Liu, M. Tian, X. Jia, E. P. Jahrman, G. T. Seidler, S. Zhang, Y. Liu, Y. Zhang, C. Meng and G. Cao, *Nano Energy*, 2020, **70**, 104519.
53 Y. Wang, J. Li and Z. Wei, *J. Mater. Chem. A*, 2018, **6**, 8194–8209.
54 J. He, G. Hartmann, M. Lee, G. S. Hwang, Y. Chen and A. Manthiram, *Energy Environ. Sci.*, 2019, **12**, 344–350.
55 H. Al Salem, G. Babu, C. V. Rao and L. M. R. Arava, *J. Am. Chem. Soc.*, 2015, **137**, 11542–11545.
56 C. Liu, G. Z. Neale, J. Zheng, X. Jia, J. Huang, M. Yan, M. Tian, M. Wang, J. Yang and G. Cao, *Energy Environ. Sci.*, 2019, **12**, 2273–2285.
57 V. Petkov, P. N. Trikalitis, E. S. Bozin, S. J. L. Billinge, T. Vogt and M. G. Kanatzidis, *J. Am. Chem. Soc.*, 2002, **124**, 10157–10162.
58 C. C. Torardi, C. R. Miao, M. E. Lewittes and Z. Li, *J. Solid State Chem.*, 2002, **163**, 93–99.

59 E. Potiron, A. Le Gal La Salle, A. Verbaere, Y. Piffard, D. Guyomard and M. Tournoux, *J. Phys. Chem. Solids*, 2001, **62**, 1447–1455.

60 E. Potiron, A. Le Gal La Salle, A. Verbaere, Y. Piffard and D. Guyomard, *Electrochim. Acta*, 1999, **45**, 197–214.

61 C. L. Londoño-Calderón, C. Vargas-Hernández and J. F. Jurado, *Rev. Mex. Fis.*, 2010, **56**, 411–415.

62 S. Boukhalfa, K. Evanoff and G. Yushin, *Energy Environ. Sci.*, 2012, **5**, 6872–6879.

63 J. Yao, Y. Li, R. C. Massé, E. Uchaker and G. Cao, *Energy Storage Materials*, 2018, **11**, 205–259.

64 J. Lee, S. Badie, P. Srimuk, A. Ridder, H. Shim, S. Choudhury, Y. C. Nah and V. Presser, *Sustainable Energy Fuels*, 2018, **2**, 577–588.

65 Y. Deng, A. D. Handoko, Y. Du, S. Xi and B. S. Yeo, *ACS Catal.*, 2016, **6**, 2473–2481.

66 J. F. Xu, W. Ji, Z. X. Shen, W. S. Li, S. H. Tang, X. R. Ye, D. Z. Jia and X. Q. Xin, *J. Raman Spectrosc.*, 1999, **30**, 413–415.

67 H. Hagemann, H. Bill, W. Sadowski, E. Walker and M. François, *Solid State Commun.*, 1990, **73**, 447–451.

68 J. Livage, *Chem. Mater.*, 1991, **3**, 578–593.

69 G. H. Jaffari, A. Tahir, M. Bah, A. Ali, A. S. Bhatti and S. I. Shah, *J. Phys. Chem. C*, 2015, **119**, 28182–28189.

70 E. Hryha, E. Rutqvist and L. Nyborg, *Surf. Interface Anal.*, 2012, **44**, 1022–1025.

71 M. Demeter, M. Neumann and W. Reichelt, *Surf. Sci.*, 2000, **454–456**, 41–44.

72 C. Li, P. Zheng, J. Li, H. Zhang, Y. Cui, Q. Shao, X. Ji, J. Zhang, P. Zhao and Y. Xu, *Angew. Chem., Int. Ed.*, 2003, **42**, 5063–5066.

73 D. Barreca, A. Gasparotto and E. Tondello, *Surf. Sci. Spectra*, 2007, **14**, 41–51.

74 http://www.xpsfitting.com/2012/01/copper.html.

75 C. Liu, C. Zhang, H. Fu, X. Nan and G. Cao, *Adv. Energy Mater.*, 2017, **7**, 1601127.

76 D. Guo, Z. Wu, Y. An, X. Li, X. Guo, X. Chu, C. Sun, M. Lei, L. Li, L. Cao, P. Li and W. Tang, *J. Mater. Chem. C*, 2015, **3**, 1830–1834.

77 https://xpssimplified.com/elements/copper.php.

78 G. T. Seidler, D. R. Mortensen, A. J. Remesnik, J. I. Pacold, N. A. Ball, N. Barry, M. Styczinski and O. R. Hoidn, *Rev. Sci. Instrum.*, 2014, **85**, 113906.

79 E. P. Jahrman, W. M. Holden, A. S. Ditter, D. R. Mortensen, G. T. Seidler, T. T. Fister, S. A. Kozimor, L. F. J. Piper, J. Rana, N. C. Hyatt and M. C. Stennett, *Rev. Sci. Instrum.*, 2019, **90**, 024106.

80 G. A. Horrocks, E. J. Braham, Y. Liang, L. R. De Jesus, J. Jude, J. M. Velázquez, D. Prendergast and S. Banerjee, *J. Phys. Chem. C*, 2016, **120**, 23922–23932.

81 Y. Li, J. Yao, E. Uchaker, J. Yang, Y. Huang, M. Zhang and G. Cao, *Adv. Energy Mater.*, 2013, **3**, 1171–1175.

82 J. Meng, Z. Yang, L. Chen, H. Qin, F. Cui, Y. Jiang and X. Zeng, *Mater. Today Energy*, 2020, **15**, 100370.

83 W. Wang and D. B. Breisinger, *Metall. Mater. Trans. B*, 1998, **29**, 1157–1166.

84 https://www.webelements.com/atom_sizes.html.

85 P. Sheng, C. Y. Wang, S. P. Jiang, X. Sun and J. Zhang, *Electrochemical Energy: Advanced Materials and Technologies*, CRC Press, 2015.

86 Y. Zhou, S. Sun, C. Wei, Y. Sun, P. Xi, Z. Feng and Z. J. Xu, *Adv. Mater.*, 2019, **31**, 1902509.

87 C. Liu, S. Wang, C. Zhang, H. Fu, X. Nan, Y. Yang and G. Cao, *Energy Storage Materials*, 2016, **5**, 93–102.

88 N. Zhang, F. Cheng, J. Liu, L. Wang, X. Long, X. Liu, F. Li and J. Chen, *Nat. Commun.*, 2017, **8**, 405.

89 L. Zhang, L. Chen, X. Zhou and Z. Liu, *Adv. Energy Mater.*, 2015, **5**, 1400930.

90 C. Liu, H. Fu, Y. Pei, J. Wu, V. Pisharodi, Y. Hu, G. Gao, R. J. Yang, J. Yang and G. Cao, *J. Mater. Chem. A*, 2019, **7**, 7831–7842.